







RESEARCH ARTICLE | AUGUST 16 2024

# Linewidth narrowing in self-injection locked lasers: Effects of quantum confinement

Artem Prokoshin ; Weng W. Chow ; Bozhang Dong; Frederic Grillot ; John Bowers ; Yating Wan  


APL Photonics 9, 086106 (2024)

<https://doi.org/10.1063/5.0214254>

CHORUS


View  
Online

Export  
Citation

## Articles You May Be Interested In

On quantum-dot lasing at gain peak with linewidth enhancement factor  $\alpha_H = 0$ 


APL Photonics (February 2020)

Extraction of inhomogeneous broadening and nonradiative losses in InAs quantum-dot lasers

Appl. Phys. Lett. (October 2015)

Influence of quantum-confined device fabrication on semiconductor-laser theory

J. Vac. Sci. Technol. A (March 2021)



### Your One-Stop Shop for the Best Brands in Optics

- Extensive inventory with over 34,000 products available & 2,900 new products
- Fast shipping from our 9 distribution centres around the globe
- Bringing 80+ years of optical expertise to customers worldwide


[Shop Now](#)

# Linewidth narrowing in self-injection locked lasers: Effects of quantum confinement

Cite as: APL Photon. 9, 086106 (2024); doi: 10.1063/5.0214254

Submitted: 16 April 2024 • Accepted: 30 July 2024 •

Published Online: 16 August 2024



Artem Prokoshin,<sup>1</sup> Weng W. Chow,<sup>2,a)</sup> Bozhang Dong,<sup>3</sup> Frederic Grillot,<sup>4,5</sup> John Bowers,<sup>3,6</sup> and Yating Wan<sup>1,b)</sup>

## AFFILIATIONS

<sup>1</sup> Computer, Electrical and Mathematical Sciences and Engineering Division, King Abdullah University of Science and Technology (KAUST), Thuwal 23955-6900, Kingdom of Saudi Arabia

<sup>2</sup> Sandia National Laboratories, Albuquerque, New Mexico 87185-1086, USA

<sup>3</sup> Institute for Energy Efficiency, University of California, Santa Barbara, California 93106, USA

<sup>4</sup> LTCI, Telecom Paris, Institute Polytechnique de Paris, 91120 Palaiseau, France

<sup>5</sup> Center for High Technology Materials, University of New-Mexico, Albuquerque, New Mexico 87106, USA

<sup>6</sup> Department of Electrical and Computer Engineering, University of California, Santa Barbara, California 93106, USA

<sup>a)</sup> Electronic mail: [wwchow@sandia.gov](mailto:wwchow@sandia.gov)

<sup>b)</sup> Author to whom correspondence should be addressed: [yating.wan@kaust.edu.sa](mailto:yating.wan@kaust.edu.sa)

## ABSTRACT

This paper explores the impact of gain medium on linewidth narrowing in integrated self-injection locked III-V/SiN lasers, theoretically and experimentally. We focus on the effects of carrier densities of states in zero- and two-dimensional structures due to quantum-dot and quantum-well confinement. The theoretical approach includes (a) multimode laser interaction to treat mode competition and wave mixing, (b) quantum-optical contributions from spontaneous emission, and (c) composite laser/free-space eigenmodes to describe outcoupling and coupling among components within an extended cavity. For single-cavity lasers, such as distributed feedback lasers, the model reproduces the experimentally observed better linewidth performance of quantum-dot active regions over quantum-well ones. When applied to integrated III-V/SiN lasers, our analysis indicates Hz-level linewidth performance for both quantum-dot and quantum-well gain media due to overcoming the difference in carrier-induced refractive index by incorporating a high-Q SiN passive resonator. Trade-offs are also explored between linewidth, output power, and threshold current.

© 2024 Author(s). All article content, except where otherwise noted, is licensed under a Creative Commons Attribution (CC BY) license (<https://creativecommons.org/licenses/by/4.0/>). <https://doi.org/10.1063/5.0214254>

## I. INTRODUCTION

Quantum well (QW) laser diodes are widely used in photonic products,<sup>1,2</sup> offering low power consumption, extended lifespan, light weight, and compactness. Meanwhile, quantum-dot (QD) laser diodes are increasingly recognized for their unique features arising from the zero-dimensional (0D) carrier density of states, which resemble the discrete electronic structure of atoms.<sup>3–5</sup> These diodes promise reduced threshold currents, enhanced thermal stability, and reduced sensitivity to external optical feedback and material defects.<sup>6</sup> Notably, the successful epitaxy growth on silicon-based platforms underscores their potential for broad application.<sup>7</sup>

However, both QW and QD lasers currently face challenges. When it comes to achieving narrow linewidth, QW lasers suffer from high linewidth enhancement factors (LEFs), while QD lasers are limited by inhomogeneous broadening.<sup>8–10</sup> An established technique for narrowing the linewidth of semiconductor lasers is self-injection locking (SIL), in which the laser is coupled to a high-Q cavity providing frequency-selective optical feedback. Since the first demonstration in 1998,<sup>11</sup> high-Q crystalline microring resonators have been integrated with laser diodes to produce narrow linewidth lasers,<sup>12–17</sup> alongside low-noise photonic microwave oscillators<sup>18</sup> and soliton comb generators.<sup>19,20</sup> Over the recent years, considerable effort has been concentrated on developing novel resonator geometries to

enhance the laser–resonator coupling and increase the strength of the reflected signal based on drop-port reflection,<sup>21,22</sup> hole defects,<sup>23</sup> photonic crystal ring resonators,<sup>24</sup> and intracavity Sagnac loops.<sup>25</sup>

For effective device engineering, a laser model that can predict the properties of the active medium using only epitaxial growth characteristics (such as layer structure and thickness) as inputs is beneficial. Such a model should be able to accurately predict the effects of transitioning from one-dimensional QW to three-dimensional QD carrier confinement without relying on phenomenological or fitting parameters. Distinguishing between intrinsic and extrinsic effects is crucial; the former helps guide engineering design, while the latter indicates the quality of growth and fabrication. This approach surpasses traditional models based on rate equations for class B lasers,<sup>26–28</sup> which combine intrinsic and extrinsic factors to reduce input parameters to the gain coefficient and LEF. While the simplification facilitates fitting to experimental data, a model that offers predictive capabilities and ties directly to the band structure is more valuable for understanding the physical principles and enhancing the device performance.

Section II presents the theoretical framework for laser operation. The approach starts with describing laser fields using cavity modes, establishing a link to quantum-mechanical theory via electron–hole polarization. These modes are explored for both single and composite cavity lasers. Following this, this paper outlines the microscopic gain theory, derived from quantum mechanics, to compute parameters in the gain region. Subsequently, the multimode laser equations are introduced, which comprise a system of coupled differential equations for the intensities and relative phases of each cavity mode. In Sec. III, this multimode laser theory is applied to analyze single-cavity QW and QD lasers, reproducing experimental results, such as the L–I curve and the linewidth–current curve. In Sec. IV, the model is extended to QW and QD lasers coupled to a high-Q resonator, examining linewidth narrowing in self-injection locked configurations.<sup>29,30</sup>

## II. THEORY

### A. Composite-cavity modes

We assume that the transverse dependence of the laser field is described by an index-guided mode  $v(x, y)$  defined by a waveguide or heterostructure. The total electric field is then expressed as  $\mathcal{E}(x, y, z, t) = v(x, y)E(z, t)$ , and the longitudinal laser field  $E(z, t)$  obeys the following equation:

$$\left( \frac{\partial^2}{\partial z^2} + \frac{n^2(z)}{c^2} \frac{\partial^2}{\partial t^2} - \frac{\alpha(z)}{c} \frac{\partial}{\partial t} \right) E(z, t) = -\mu_0 \frac{\partial^2}{\partial t^2} P(z, t), \quad (1)$$

where  $t$  is the time,  $z$  is the position along the cavity, and  $\mu_0$  and  $c$  are the permeability and speed of light in vacuum. Losses due to intracavity absorption are described by  $\alpha(z)$ , the refractive index profile is given by  $n(z)$ , and  $P(z, t)$  is the polarization representing the active medium. Next, we expand  $E(z, t)$  and  $P(z, t)$  in terms of the cavity eigenmodes  $u_n(z)$ ,

$$E(z, t) = \frac{1}{2} e^{-i\Omega_0 t} \sum_n E_n(t) e^{-i\phi_n(t)} u_n(z) + \text{c.c.}, \quad (2)$$

$$P(z, t) = \frac{1}{2} e^{-i\Omega_0 t} \sum_n P_n(t) e^{-i\phi_n(t)} u_n(z) + \text{c.c.}, \quad (3)$$

where  $E_n$  and  $P_n$  are slowly varying amplitudes,  $\Omega_0$  is the central lasing frequency, and  $\phi_n$  is the phase of the field in each mode. The equation for modes  $u_n$  of the passive cavity (i.e., no gain and loss) is obtained from Eq. (1) by setting  $\partial^2 P / \partial t^2 = \alpha(z) = 0$  and  $E(z, t) = E_n \cos(\Omega_n t) u_n(z)$ ,

$$\frac{d^2}{dz^2} u_n(z) = -\frac{n^2(z)}{c^2} \Omega_n^2 u_n(z), \quad (4)$$

where  $\Omega_n$  is the passive-cavity frequency. The refractive index of the SiN resonator is  $n_r = 2.0$ , and that of the laser cavity is  $n_l = 3.4$ .

We treat the integrated laser and free space as a combined optical system,<sup>31–33</sup> providing a framework applicable for arbitrary optical coupling between the laser and the resonator, as well as between the laser and free space. In addition, it allows a more rigorous derivation of the laser equations by providing an orthonormal basis for an open laser cavity and also accommodating modal projections leading to laser equations.

The composite cavity/free-space approach is based on extending the effective refractive index  $n(z)$  in Eq. (3) to include a very long cavity approximating free space. For the laser/free space system sketched in Fig. 1(a), the composite-cavity modes are obtained by solving Eq. (4) with the following boundary conditions:<sup>34</sup>

$$u_n(z_0) = u_n(z_2) = 0, \quad (5)$$

$$u_n(z_1^+) = u_n(z_1^-), \quad (6)$$

$$\frac{d}{dz} u_n(z_1^+) - \frac{d}{dz} u_n(z_1^-) = -2\sqrt{\frac{1-T_1}{T_1}} k u_n(z_1), \quad (7)$$

where  $z_0$  and  $z_2$  are the left and right boundary points,  $z_1^-$  and  $z_1^+$  are located immediately prior to and after the facet with transmission  $T_1$ , and  $k$  is the average magnitude of the wave vector. The outcoupling from a coated cleaved facet or DBR is treated as a refractive index “bump,” giving an effective transmission  $T_1$ , i.e., an additional term is added into the refractive index as follows:  $n'^2(z) = n^2(z)(1 + \Lambda \delta(z - z_1))$ , where  $\Lambda = \frac{2}{k} \sqrt{\frac{1-T_1}{T_1}}$ . The length of  $L_2$  is chosen to be sufficiently long to resolve the Fox–Li quasi-mode.<sup>35</sup> Integrating Eq. (4) by parts leads to an orthogonality relation,

$$\int dz n^2(z) u_n(z) u_m(z) = N_c \delta_{nm}, \quad (8)$$

where  $N_c = \sum_j n_j L_j$  is a normalization constant. Figure 1(a) shows a cavity/free space system used to describe single-cavity lasers. The corresponding resonance spectrum is shown in Fig. 1(c), with the horizontal axis corresponding to the frequency relative to the central optical frequency and the vertical axis being the laser cavity longitudinal confinement factor,

$$\Gamma_{nm,l} = N_c^{-1} \int_{\text{laser}} dz n^2(z) u_n^2(z), \quad (9)$$

where the “ $l$ ” in the subscript denotes the laser cavity and the integration is performed over the laser cavity. We also introduce the nonlinear confinement factor as

$$\Gamma_{nm}^{(3)} = N_c^{-1} \int_{\text{laser}} dz n^2(z) u_n^2(z) u_m^2(z). \quad (10)$$

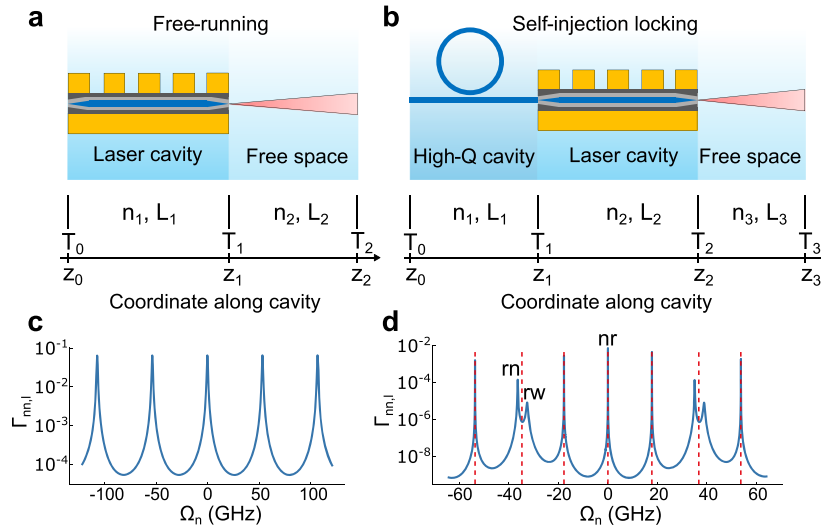


**FIG. 1.** (a) Free-running laser/free space system and (c) corresponding cavity resonances. (b) High-Q cavity/laser/free space setup and (d) corresponding cavity resonances, displaying three distinct types of peaks: resonant narrow (rn), resonant wide (rw), and non-resonant (nr). The resonances of the high-Q cavity are shown in red.

Both the linear and nonlinear mode confinement factors have roles in calculating the laser parameters below.

This approach can also be applied to self-injection locked lasers, i.e., lasers coupled to a high-Q resonator. Ideally, to derive the coupled laser/resonator passive-cavity eigenfunctions, one should solve the homogeneous (i.e., without the active medium) Maxwell's equations with exactly the spatial dependence of refractive index describing different material layers, such as distributed Bragg reflectors, spacers, and waveguides. Addressing this complexity typically requires the use of advanced finite-difference time-domain (FDTD) techniques and extending to two or three dimensions.<sup>36</sup> Here, we take advantage of the fact that the passive-cavity and laser-physics calculations can be conducted independently. This allows flexibility to simplify the passive-cavity analysis while still providing accurate passive-cavity input to the laser-physics calculations, particularly for addressing fundamental band structure questions. With this assumption, we proceed with an equivalent 1D arrangement of optically coupled laser and resonator cavities [Fig. 1(b)]. Equation (4) is solved, taking into account cavity lengths and interface transmissions [ $L_n$  and  $T_n$ , Fig. 1(b)] to achieve the desired uncoupled laser cavity and high-Q resonator resonances characterized by their linewidths,

$$\Delta\Omega_{\text{laser}} = -\frac{c}{2L_2n_2} \ln[(1-T_1)(1-T_2)], \quad (11)$$

$$\Delta\Omega_{\text{resonator}} = -\frac{c}{2L_1n_1} \ln(1-T_1). \quad (12)$$

The solution is repeated for the coupled cavities, with the effective transmission  $T_1$  determining the coupling between the laser and resonator cavities. The resonance spectrum is shown in Fig. 1(d), and the confinement factor is plotted vs the relative passive-mode frequency  $\Omega_n - \Omega_0$ . The customary mode confinement

factor describing the overlap of the gain region with the optical mode within the laser cavity is  $\Gamma_{nm,l}^{(1)}/(\Gamma_{nm,l}^{(1)} + \Gamma_{nm,r}^{(1)})$ , where  $\Gamma_{nm,l}^{(1)} = N_c^{-1} \int_{\text{resonator}} dz n^2(z) u_n(z) u_n(z)$ . Each resonance is composed of multiple composite-cavity modes, yielding a finite linewidth  $\Delta_{\text{cav}}$  due to the free-space coupling. The coupled-cavity plot shows three types of resonances. At points where the uncoupled cavity resonances align, there are two closely spaced composite-cavity resonances (rn and rw), with their splitting determined by the coupling  $T_1$ . The other resonances (such as nr) originate from the eigenmodes of the longer resonator cavity and are observable in the laser cavity due to optical coupling. We note that the optical phase between the laser and resonator cavity has an important effect on laser linewidth<sup>27</sup> and determines the operating regime, leading to the generation of frequency combs at certain values of the phase.<sup>37,38</sup> In this work, the phase is fixed at the optimal value for SIL operation.

## B. Gain calculations

The microscopic, or quantum-mechanical, polarization  $p_q(t)$  is obtained by solving semiconductor Bloch equations, which are in turn obtained as Heisenberg operator equations using a Hamiltonian for electrons and holes interacting with a radiation field (Sec. 3 of Ref. 39). The macroscopic polarization for each of the modes is then obtained as

$$P_n(t) = \frac{2\Gamma_{\perp}\wp}{V_{\text{mode}}} \sum_q e^{i\Omega_0 t + i\phi_n(t)} \frac{2}{L} \int_0^L dz u_n(z) p_q(t), \quad (13)$$

where  $\Gamma_{\perp}$  is the transverse mode confinement factor,  $\wp$  is the dipole matrix element for the interaction between the electron-hole pair and the laser field,  $V_{\text{mode}}$  is the mode volume, and  $L$  is the extension of  $u_n(z)$ .

### C. Laser dynamics

Substituting Eqs. (2) and (3) into Eq. (1) gives the following equations for mode amplitudes and phases:

$$\frac{d}{dt}E_n = -\frac{\gamma_n^{\text{cav}}}{2}E_n - \frac{\Omega_0}{2\varepsilon_B}\text{Im}(P_n), \quad (14)$$

$$\frac{d}{dt}\phi_n = \Omega_n - \Omega_0 - \frac{\Omega_0}{2\varepsilon_B}\frac{1}{E_n}\text{Re}(P_n). \quad (15)$$

The composite-cavity mode loss rate  $\gamma_n^{\text{cav}}$  is defined through the linear mode confinement factors as

$$\gamma_n^{\text{cav}} = \frac{c}{n_B} \sum_k \alpha_k^{\text{abs}} \Gamma_{nm,k}, \quad (16)$$

where summation is over all cavities in the system,  $\alpha_k^{\text{abs}}$  is the absorption coefficient in the  $k$ th cavity, and  $n_B$  is an average background refractive index.

Then, we calculate  $p_q(t)$  to third order in electron–light interaction, substitute the results into Eq. (13), and from Eqs. (14) and (15), obtain the following equations for the slowly varying intensity and phase of each cavity mode:

$$\frac{dI_n}{dt} = [g_n^{\text{sat}}(N) - \gamma_n^{\text{cav}}]I_n + S_n(N) + \sum_{m \neq n} 2\sqrt{I_n I_m} \text{Re}[B_{nm}(N)e^{-i\psi_{nm}}], \quad (17)$$

$$\begin{aligned} \frac{d\phi_n}{dt} = & \Omega_n - \Omega_0 + \left[ \sigma_n(N) - \sum_m \tau_{nm}(N)I_m \right] \\ & + iS_n^{\phi}(N) + \sum_{m \neq n} \sqrt{\frac{I_m}{I_n}} \text{Im}[B_{nm}(N)e^{-i\psi_{nm}}], \end{aligned} \quad (18)$$

where we introduced the new variables  $I_n = [\wp E_n / (2\hbar\gamma)]^2$ ,  $\psi_n = \phi_n + \Omega_n t$ , and  $\psi_{nm} = \psi_n - \psi_m$ . On the right-hand side of Eqs. (17) and (18),  $g_n^{\text{sat}}$  is the saturated gain, and  $\sigma_n$  and  $\tau_{nm}$  are the frequency pulling and pushing coefficients, which describe the effect of carrier-induced refractive index change and cause the deviation of the lasing frequency from the cavity frequency  $\Omega_n$ . In addition, the frequency locking terms containing the coefficients  $B_{nm}$  and phase differences  $\psi_{nm}$  provide a distinctive influence in composite cavity lasers. They play a crucial role in laser spectral behavior by locking the laser to the high-Q resonator. The spontaneous emission contributions, denoted as  $S_n$  and  $S_n^{\phi}$ , are obtained from a cavity quantum electrodynamics (cQED) analysis for a single cavity mode.<sup>40</sup> Table I contains the expressions for the quantities introduced in Eqs. (17) and (18). Unlike gas and solid-state lasers, where active medium coefficients are evaluated with unsaturated populations, here, all active medium coefficients are calculated at the saturated carrier density  $N$  due to rapid carrier scattering. Equations (17) and (18) are solved simultaneously with the carrier density equation of motion,

$$\frac{dN}{dt} = \frac{\varepsilon_B \hbar Q_W}{8\hbar \Omega_0 \Gamma_{\perp}} \left( \frac{\wp}{2\hbar\gamma} \right)^2 \sum_n g_n^{\text{sat}} I_n + \frac{\eta J}{en_{QW}} - \gamma_{\text{nr}} N - B_{\text{sp}} N^2, \quad (19)$$

where the variables are defined in Table I. In addition, in Table I,  $F_1 = \wp^2 \Omega_0 n_{QW} / (2\hbar\gamma\varepsilon_B \hbar Q_W)$ ,  $D_y(x) = \frac{y}{y+ix}$ ,  $L_y(x) = \frac{y^2}{y^2+x^2}$ ,  $w$  and  $L_g$  are the active region width and length,  $\beta$  is the spontaneous emission factor,  $\gamma_{ab}$  is the carrier population relaxation rate, and  $f(\varepsilon_{e,q}, \mu_e, T)$  and  $f(\varepsilon_{h,q}, \mu_h, T)$  are the electron and hole populations, with chemical potentials  $\mu_e$  and  $\mu_h$  at temperature  $T$ .

**TABLE I.** Active medium coefficients.

Parameter	Equation
Small-signal gain	$g_n = 2 \text{Re}[F_1 \Gamma_{\perp} \Gamma_{nn,l}^{(1)} \Lambda_n^{(1)} N_{\text{inv}}]$
Saturated gain	$g_n^{\text{sat}} = \frac{g_n}{1 + \sum_m \kappa_{nm} I_m}$
Frequency pulling	$\sigma_n = \text{Im}[F_1 \Gamma_{\perp} \Gamma_{nn,l}^{(1)} \Lambda_n^{(1)} N_{\text{inv}}]$
Population inversion	$N_{\text{inv}} = f(\varepsilon_{e,q}, \mu_e, T) + f(\varepsilon_{h,q}, \mu_h, T) - 1$
Frequency locking	$B_{nm} = F_1 \Gamma_{xy} \Gamma_{nn,l}^{(1)} \Lambda_m^{(1)} N_{\text{inv}}$
Gain compression	$\kappa_{nm} = \frac{2\gamma \Gamma_{nm}^{(3)} \text{Re}(\Lambda_{nm}^{(3)})}{\gamma_{ab} \Gamma_{nn,l}^{(1)} \text{Re}(\Lambda_n^{(1)})}$
Frequency pushing	$\tau_{nm} = 2F_1 \Gamma_{nm}^{(3)} \text{Im}(\Lambda_{nm}^{(3)}) \gamma / \gamma_{ab}$
Linear susceptibility	$\Lambda_n^{(1)} = \sum_q D_y(\Omega_n - \omega_q)$
Nonlinear susceptibility, diagonal	$\Lambda_{nn}^{(3)} = \sum_q D_y(\Omega_n - \omega_q) L_y(\Omega_n - \omega_q)$
Nonlinear susceptibility, off-diagonal	$\Lambda_{nm}^{(3)} = \frac{\gamma}{\gamma_{ab}} \sum_q D_y(\Omega_n - \omega_q) \times [2L_y(\Omega_m - \omega_q) + D_{\gamma_{ab}}(\Omega_n - \Omega_m) \times (D_y(\Omega_n - \omega_q) + D_y(\Omega_q - \omega_m))]$
Spontaneous emission, intensity	$S_n = \frac{\varepsilon_0 n_{QW} w L_g}{\varepsilon_B V_{\text{mode}}} \left( \frac{\wp}{2\hbar\gamma} \right)^2 \Gamma_{nn,l}^{(1)} \times \beta B_{\text{sp}} f(\varepsilon_{e,n}, \mu_e, T) f(\varepsilon_{h,n}, \mu_h, T)$
Spontaneous emission, phase	$S_n^{\phi} = \gamma_n^{\text{cav}} \frac{\varepsilon_B V_{\text{mode}}}{2\hbar v_n} \left( \frac{\wp}{2\hbar\gamma} \right)^2 \frac{1}{I_n}$

**TABLE II.** QD and QW DFB laser parameters with values based on devices we fabricated. The QD active region consists of  $\text{In}_{0.15}\text{Ga}_{0.85}\text{As}$  QWs embedding  $\text{InAs}$  QDs. The QW active region consists of  $\text{In}_{0.68}\text{Al}_{0.06}\text{Ga}_{0.26}\text{As}$  QWs.

Parameter	Symbol	QW	QD
QW height	$h_{\text{QW}}$ (nm)	6	9
Waveguide height	$h_{\text{wg}}$ ( $\mu\text{m}$ )	0.214	0.88
Stripe width	$w$ ( $\mu\text{m}$ )	4	3
Cavity length	$L_g$ ( $\mu\text{m}$ )	200	800
Number of QWs	$n_{\text{QW}}$	7	5
QD density	$N_{\text{QD}}$ ( $\text{m}^{-2}$ )	...	$4 \times 10^{14}$
Inhomogeneous broadening	$\Delta_{\text{inh}}$ (meV)	...	10
Dephasing rate	$\gamma$ ( $\text{s}^{-1}$ )	$10^{12}$	$10^{12}$
Bimolecular recombination rate	$B_{3d}$ ( $\text{m}^3 \text{s}^{-1}$ )	$10^{-16}$	$10^{-16}$
Defect loss rate	$\gamma_{\text{nr}}$ ( $\text{s}^{-1}$ )	$10^8$	$2 \times 10^9$
Carrier injection efficiency	$\eta$	0.7	0.7

After numerically solving Eqs. (17)–(19), we obtain a time-dependent total output electric field of the laser,

$$E(t) = \sum_n \sqrt{I_n(t)} e^{i\psi_n(t)}. \quad (20)$$

According to the Wiener–Khinchin theorem, the lasing spectrum can be determined by Fourier transforming the autocorrelation function

$$\tilde{S}(f, t) = \int_0^{+\infty} d\tau E(t + \tau) E(t) e^{2\pi i f \tau}. \quad (21)$$

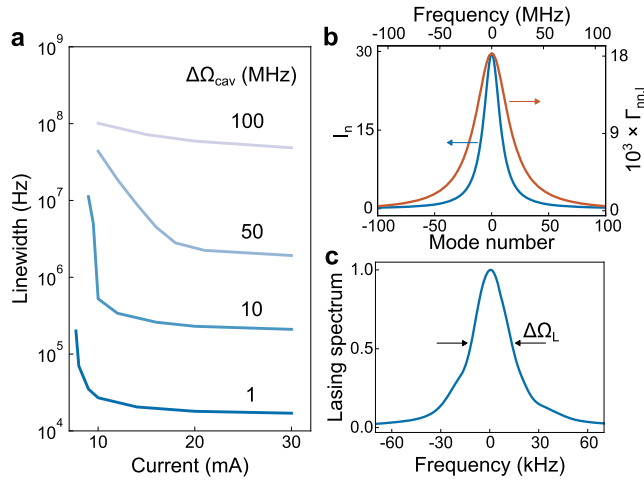


**FIG. 2.** (a) Calculated full-width at half maximum (FWHM) of the lasing spectrum vs injection current for a QD single-cavity laser. The passive cavity linewidth  $\Delta\Omega_{\text{cav}}$  for each curve is indicated. The curves depict the FWHM of the time-averaged lasing spectrum  $S(f)$ . (b) The blue curve shows the intensity of composite-cavity modes at twice the lasing threshold. The x-axis indicates the composite-cavity mode number (bottom) and mode frequency  $\Omega_n - \Omega_0$  (top). The orange curve shows the cavity resonance for comparison. (c)  $S(f)$  computed for  $\Delta\Omega_{\text{cav}} = 50$  MHz and 30 mA injection current.

The time-averaged lasing spectrum is obtained by averaging over time  $T$ ,

$$S(f) = \frac{1}{T} \int_t^{t+T} d\tau \tilde{S}(f, \tau). \quad (22)$$

### III. SINGLE CAVITY LASERS

We first apply the theory to single-cavity lasers, such as lasers with cavities formed by cleaved facets or distributed Bragg reflectors. Table II lists the laser parameters used in the simulations, which are characteristic of the experimental devices with which we will be comparing the results.<sup>41–44</sup> For QD lasers, the summation over transition energies in the quantities given in Table I is replaced by an integration over the QD transition energies  $\varepsilon_q = \hbar\omega_q$  to account for the inhomogeneous population distribution of quantum dots,

$$\frac{1}{A} \sum_q \rightarrow \frac{2N_{\text{QD}}}{\sqrt{2\pi}\Delta_{\text{inh}}} \int_{-\infty}^{+\infty} d\varepsilon_q \exp\left[-\left(\frac{\varepsilon_q}{\sqrt{2}\Delta_{\text{inh}}}\right)^2\right], \quad (23)$$

where  $\Delta_{\text{inh}}$  is the inhomogeneous broadening width and  $N_{\text{QD}}$  is the QD density per layer (in  $\text{cm}^{-2}$ ). From electronic structure calculations, the dipole matrix element  $\varphi = e \times 0.6$  nm, and the electron and hole confinement energies are 100 and 60 meV, respectively. The

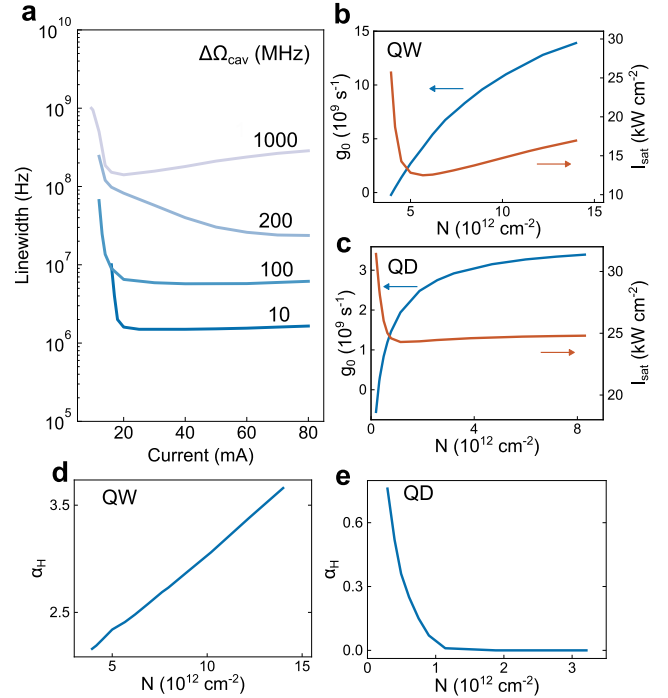


**FIG. 3.** (a) Calculated full-width at half maximum (FWHM) of the lasing spectrum vs injection current for a QW single-cavity laser. The passive cavity linewidth  $\Delta\Omega_{\text{cav}}$  for each curve is indicated. The curves depict the FWHM of the time-averaged lasing spectrum  $S(f)$ . (b) Peak gain (blue) and gain compression factor (orange) vs carrier density for QW laser. (d) Linewidth enhancement factor vs carrier density for QW laser. (c) and (e) Same for the QD laser.



confinement energies are from the QW band edges to the center of the QD inhomogeneous distribution.

For the QW case, summation over states is replaced by integration over the two-dimensional conduction and valence bands,

$$\frac{1}{A} \sum_q \rightarrow \frac{1}{\pi} \int_0^{+\infty} dk \, k, \quad (24)$$

where  $k$  is the carrier momentum and  $A$  is the QW area. The dipole matrix element is  $\wp = e \times 0.4$  nm, and the electron and hole confinement energies are 60 and 40 meV, respectively. The confinement energies are from the QW band edges to the band edges of the bulk cladding layers.

Figure 2(a) shows the dependence of linewidth of a QD DFB laser on the injection current for different passive-cavity linewidths  $\Delta\Omega_{\text{cav}}$ , and Fig. 3(a) shows the same for a QW DFB laser. Two mechanisms contribute to the linewidth narrowing. The first is gain clamping, as in the Schawlow–Townes laser linewidth treatment, where the saturated gain  $g_n^{\text{sat}}$  remains pegged to the cavity loss rate  $\gamma_n^{\text{cav}}$  after threshold is reached.<sup>45</sup> This appreciably reduces the number of composite-cavity modes contributing to the emission, as shown in Fig. 2(b), where the orange curve corresponds to the cavity resonance shape and the blue curve corresponds to mode intensity at twice the lasing threshold. There is a second mechanism described by the term in Eq. (18) containing the relative phase  $\psi_{nm}$ . It tends to lock the composite-cavity modes to a common frequency, i.e.,  $d\psi_{nm}/dt = 0$  for all lasing modes. However, all simulations for single-cavity lasers show only partial locking, which produces a  $\delta(f, t)$  with time-varying width and spectral position. The resulting time-averaged lasing spectrum is shown in Fig. 2(c).

There are important quantitative differences between the QW and QD cases. Linewidth narrowing in QW single-cavity lasers saturates around the MHz level [Fig. 3(a)], while linewidth narrowing in QD single-cavity lasers saturates considerably lower, around tens of kHz. The difference, as indicated by comparing Figs. 3(d) and 3(e), is due to the significantly smaller frequency pulling coefficient  $\sigma_n$  in QD lasers, resulting in a considerably reduced LEF, given by  $\alpha_H = 2\sigma_n/g_n$ , with the unsaturated gain and saturation intensity shown in Figs. 3(b) and 3(c).

Implementing the microscopic (quantum-mechanical) approach is greatly facilitated by the fact that active medium coefficients are determined solely by the gain structure and are independent of the cavity configuration. This allows one to leverage data from well-established laser systems, such as QD and QW DFB lasers, to gain insights into the III–V section. In particular, the spectral overlaps  $\Lambda_{nm}^{(1)}$  and  $\Lambda_{nm}^{(3)}$  depend on the electronic levels and the polarization dephasing rate  $\gamma$ . We obtain the electronic structure from band structure calculations given the epitaxial growth sheet. The gain compression factors calculated from the third order electron–hole polarization are consistent with the four-wave mixing coefficients extracted in pump–probe experiments.<sup>46</sup> Further confirmation comes from the comparisons between theory and experimental studies of mode-locked pulse and RF spectra in self-mode-locked InAs QD lasers.<sup>47</sup> The carrier scatter rate  $\gamma$  is determined by fitting the linear gain  $g_n$  vs carrier density curve (calculated using the formula in Table I) to predictions from many-body theory, where scattering is addressed through quantum kinetic

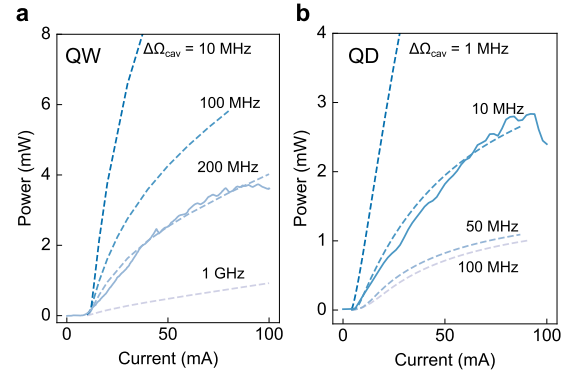


**FIG. 4.** Experimental and calculated (solid and dashed) L–I curves for (a) QW and (b) QD active regions. The values listed in Table II for parameters describing sample quality (injection efficiency and defect loss) are obtained by fitting the experimental data with  $\Delta\Omega_{\text{cav}} = 10$  MHz for the QD and  $\Delta\Omega_{\text{cav}} = 200$  MHz for the QW.

equations.<sup>39,48</sup> Extending this comparative analysis with lasers of different lengths offers insights into inhomogeneous broadening.<sup>41</sup> Interestingly, the extracted QD and QW scattering rates are similar, a prediction affirmed by quantum kinetic calculations because of the balancing among different Coulomb correlation contributions.<sup>49</sup> It means that the distinctions observed between QD and QW integrated III–V/Si lasers arise solely from the differences between zero-dimensional vs two-dimensional carrier densities of states. The other sample-dependent extrinsic parameters (injection efficiency and defect loss) are extracted by reproducing the measured L–I curves from our fabricated QD and QW DFB lasers (Fig. 4).<sup>41,42</sup> The output power is computed as

$$P = \frac{\gamma_{\text{out}} \epsilon_B V_{\text{mode}}}{4} \left( \frac{\wp}{2\hbar\gamma} \right)^{-2} \sum_n \Gamma_{nn}^{(1)} I_n, \quad (25)$$

where  $\gamma_{\text{out}} = -c \ln(1 - T_1)/(2L_1 n_1)$ . For the fits, we assume passive cavity linewidths  $\Delta\Omega_{\text{cav}} = 10$  and 100 MHz, respectively, for the QD and QW lasers. The choices are made based on the measured QD and QW linewidths of 26 kHz and 7.16 MHz, respectively.<sup>43,50</sup> Figures 4(a) and 4(b) show those values to fall between  $\Delta\Omega_{\text{cav}} = 1$ –10 MHz for the QD laser and very close to  $\Delta\Omega_{\text{cav}} = 200$  MHz for the QW laser. The other calculations are performed using the same extracted parameter values.

#### IV. SELF-INJECTION LOCKED LASERS

This section discusses the laser linewidth when a high-Q resonator is optically coupled to the QD or QW DFB lasers, as modeled in the previous section. Figures 5(a) and 5(b) show the computed spontaneous emission limited lasing linewidth vs injection current for the QW and QD lasers described by the parameters in Table II. The passive-cavity linewidths  $\Delta\Omega_{\text{cav}} = 1$  GHz, 100 MHz, and 10 MHz are obtained by lasing at the rw, rn, and nr resonances, respectively, with  $L_1 = 3$  mm,  $T_1 = 0.040$ ,  $T_2 = 0.035$ . For  $\Delta\Omega_{\text{cav}} = 100$  and 10 MHz, both QD and QW lasers exhibit significant linewidth narrowing to less than  $10^{-6} \times \Delta\Omega_{\text{cav}}$ , which is a significant improvement over the single-cavity results. The similarity in linewidths for QW

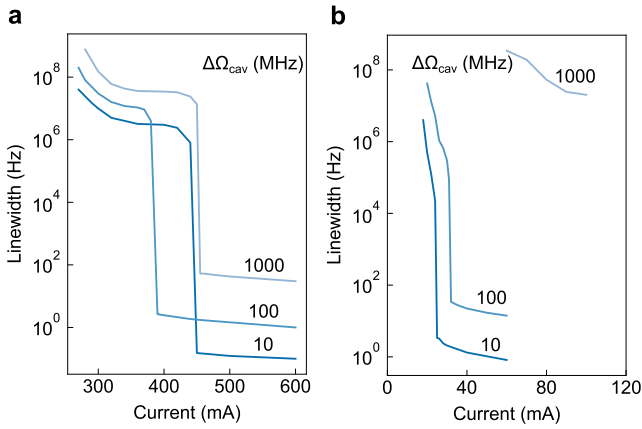


**FIG. 5.** Calculated spontaneous emission limited linewidth vs injection current for the SIL lasers with (a) QW and (b) QD active media.

and QD lasers suggests that the SiN cavity can mitigate the carrier-induced refractive index, facilitating complete frequency locking of the composite-cavity modes and, thus, defining the linewidth solely by  $S_n^\phi$ . Conversely, the  $\Delta\Omega_{\text{cav}} = 1$  GHz curve in Fig. 5(b) does not show the same significant linewidth narrowing as in the other scenarios. Examination of the input–output (L–I) dependence indicates that intracavity intensity must be sufficiently high to achieve complete frequency locking.

Phase dynamics, as governed by Eq. (18), plays an equally important role in linewidth narrowing as gain clamping. Within the range of injection current where significant linewidth narrowing occurs, partial frequency locking leads to both QD and QW

lasers exhibiting complex dynamical behaviors that are related to those observed and predicted for self-injection locking.<sup>19,51</sup> To illustrate this, we track the time dependencies of the lasing frequencies,  $d\psi_n/dt$ , in composite-cavity modes  $n = 0, \pm 2, \pm 4, \pm 6$  in the QD laser with  $\Delta\Omega_{\text{cav}} = 100$  MHz. At 24 mA, the time traces show significant fluctuation, with  $d\psi_n/dt$  spiking randomly [Fig. 6(a), top]. The resulting time-averaged spectrum has a linewidth of  $\Delta\Omega_L = 5$  MHz [Fig. 6(a), bottom]. A noticeable change in dynamical behavior occurs at the slightly higher injection current of 26 mA. The time traces in Fig. 6(b) indicate a focusing of  $d\psi_n/dt$  traces and synchronization in the spiking. The resulting time-averaged spectrum has a linewidth of 1 MHz. For injection current values over 32 mA, complete frequency locking takes place. Figure 6(c) shows that at 100 mA, all  $d\psi_n/dt$  time traces merge, yielding a remarkably narrow laser linewidth of 10 Hz.

We also compare our model to the results of external-cavity locking (ECL) experiments, in which a 16 m long optical fiber reflector is coupled to a QD or QW laser.<sup>44</sup> This coupled-cavity configuration is highly suitable for our composite cavity model. Figure 7 shows the comparison. The extrinsic laser properties ( $\gamma_{\text{nr}} = 2 \times 10^9 \text{ s}^{-1}$ ,  $\eta = 0.7$ ,  $\Delta_{\text{inh}} = 10 \text{ meV}$  for the QD laser, and  $\gamma_{\text{nr}} = 10^8 \text{ s}^{-1}$ ,  $\eta = 0.7$  for the QW laser) are determined by fitting our model to the experimentally measured L–I curves [Figs. 7(a) and 7(b)]. With the choices of  $\Delta\Omega_{\text{cav}}$  as indicated in Figs. 7(c) and 7(d), we obtain relatively good agreement with the experiment. The hollow markers and dashed lines are for the free-running lasers, while the solid markers and solid lines are for the lasers coupled to the optical fiber.

For complex systems, such as integrated self-injection locked lasers, the vast parameter space presents numerous opportunities and challenges for design engineering.<sup>52</sup> Often, enhancing one performance parameter might compromise another. In this section, we discuss an example where our model can facilitate parametric

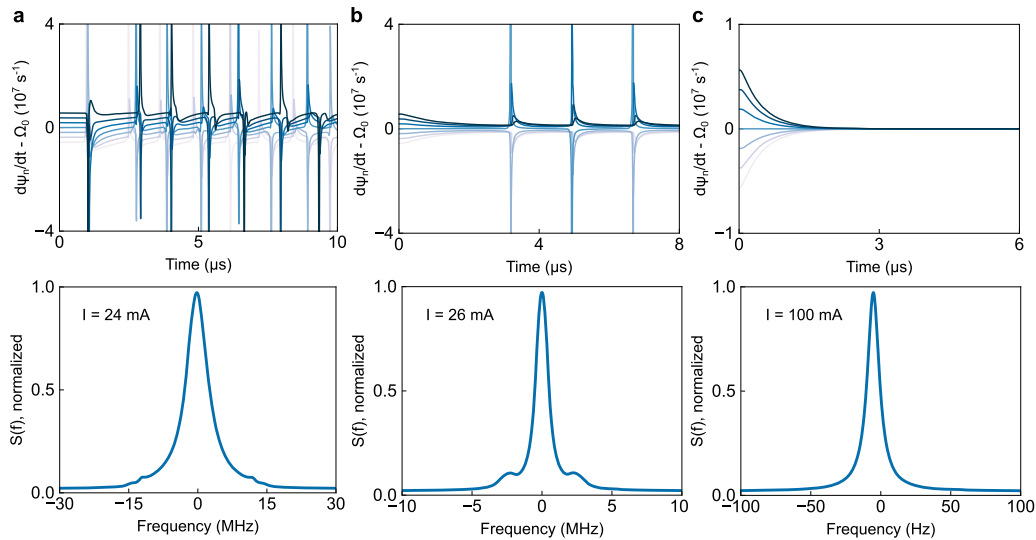


**FIG. 6.** Top: lasing frequency as a function of time for modes  $n = 0, \pm 2, \pm 4, \pm 6$  with injection current (a) 24 mA, (b) 26 mA, and (c) 100 mA. Bottom: corresponding averaged lasing spectra  $S(f)$ . The results are shown for the QD laser with  $\Delta\Omega_{\text{cav}} = 100$  MHz.



studies to yield informed design decisions, especially in applications requiring a balance between output power and narrow linewidth.

The modeling performed so far is based on gain structures from our own fabricated lasers.<sup>43,44</sup> However, the L-I curves suggest that they may not be optimal for III-V/SiN lasers. For example, fewer QW layers may lower the threshold current, as shown in Fig. 8(a). Reducing from seven to four or fewer QW layers can significantly reduce the threshold current by almost an order of magnitude. However, the downside to this reduction is a decrease in output power and the onset of L-I rollover. Furthermore, the single-QW result indicates a limit in decreasing the number of QW layers, with the linewidth plateauing at 1 MHz regardless of the injection current. Similar to the QD  $\Delta\Omega_{\text{cav}} = 1$  GHz case in Fig. 5(b), a minimum intracavity intensity is necessary to achieve the full benefits of the SiN resonator. Otherwise, the laser's behavior is akin to that with unfiltered feedback.

For the QD III-V/SiN laser, appreciable L-I rollover suggests the potential benefit of incorporating additional QD layers. Figure 8(b) indicates that increasing the number of QD layers from five enhances the output power without a significant penalty in threshold current or linewidth. Notably, the linewidth reaches Hz-level before any L-I rollover, which is beneficial to modulation speed. However, surpassing nine QD layers may introduce engineering challenges, such as maintaining current uniformity over the entire active region. Similar benefits are observed when increasing the QD density within each layer.

As is clear from Figs. 8(a) and 8(b), L-I rollover poses a constraint on output power, attributable to two primary factors. First, gain compression from spatial and spectral hole burning leads to saturation. This is accounted for in our model by performing the electron-hole polarization derivation to the third order in the light-carrier interaction. With the onset of gain compression, the carrier

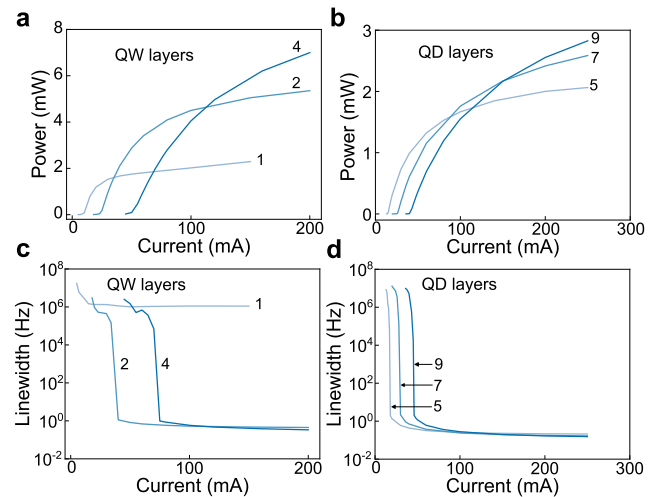


**FIG. 8.** Calculated output power and linewidth vs injection current for (a) and (c) QW and (b) and (d) QD III-V/SiN lasers. The curves are for different numbers of QW or QD layers. Lasing is assumed from a  $\Delta\Omega_{\text{cav}} = 10$  MHz nr resonance. All other parameters are listed in Table II.

population is not clamped to the threshold value but continues to increase with the increasing injection current. Second, gain saturation occurs at high carrier densities in both QW and QD gain structures. For QWs, the saturation stems from the step function carrier density of states, while in QDs, it results from both the finite density of QD and the inhomogeneous broadening, presently limited by the current epitaxial growth capability. Working together, these two factors result in the L-I rollover. Class B rate-equation treatment [see, e.g., Eq. (5.17) in Ref. 1] predicts a linear L-I behavior in the absence of ad hoc gain compression factors.

## V. CONCLUSION

This paper describes a study of the effects of the gain medium on linewidth narrowing in integrated self-injection locked III-V QW and QD lasers. The theoretical approach accounts for (a) multimode laser interaction resulting in mode competition and wave mixing, (b) the quantum-optical contributions from spontaneous emission, and (c) the coupling dynamics among optical components via composite laser/free-space eigenmodes. This extension beyond traditional rate equation models allows predictions directly connected to band structure while emphasizing the distinction between intrinsic and extrinsic effects. The former guides engineering design, while the latter indicates fabrication quality.

Applying this theory to single-cavity lasers, such as DFB, DBR, or coated-facet lasers, reveals two primary physical mechanisms for linewidth narrowing: gain clamping, as in the Schawlow-Townes model, and frequency locking of composite laser/free-space modes. For single-cavity lasers, there is only partial frequency locking, resulting in linewidths limited by frequency drifts of the lasing spectra. For integrated III-V/SiN lasers, complete frequency locking can be achieved due to the mitigation of carrier-induced refractive index with a passive high-Q cavity, thereby reaching Hz-level spontaneous emission limited linewidths for both QW and QD lasers. Parametric

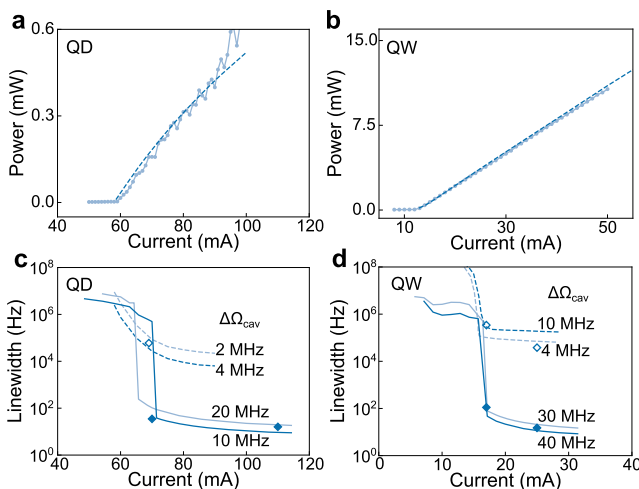


**FIG. 7.** (a) and (b) L-I curves of the QD and QW lasers used in external cavity experiments. (c) and (d) Linewidth vs current plots for the same lasers. The dashed curves are simulation data for free-running lasers, the solid curves are simulation data for cavity-locked lasers, the hollow markers are experimental data for free-running lasers, and the solid markers are experimental data for cavity-locked lasers.

studies suggest that the 2D QW carrier density of states helps achieve high output power, while the 0D QD carrier density of states benefits low threshold currents. Studies over a broad parameter space<sup>52</sup> show that integrated III–V/SiN QW and QD lasers offer complementary solutions to meet the diverse requirements of photonic applications with highly stable semiconductor lasers.

The theoretical framework is also validated with experimental data from InAs QD and InGaAsP QW DFB and DBR lasers. Recent experiments with QD and QW lasers coupled to an optical fiber in an external cavity configuration reinforce the composite mode approach for modeling coupled laser and resonator cavities. The application of cavity-QED physics has been partially validated by accurately capturing the deviation of the lasing spectrum from a Lorentzian function in nanolaser experiments.<sup>53</sup> Furthermore, the model's precision in describing III–V optical nonlinearities has been confirmed through four-wave mixing and pump–probe experiments,<sup>46</sup> as well as by reproducing the measured pulse train and RF spectrum of self-mode-locked InAs QD lasers.<sup>47</sup>

Despite these advances, our theory is still evolving. The current free-carrier gain theory, while effective in describing the differences between 3D QD confinement and 1D QW confinement, does not fully account for many-body effects. This omission may lead to inaccurate predictions, especially regarding inhomogeneous broadening and the impact of doping on QD carrier-induced refractive index. Moreover, integrating the effects of cavity-QED into semiclassical laser theory poses a challenge. Work is under way to develop a comprehensive quantum optical treatment for integrated cavity-locked lasers and to refine the strong-signal multimode description—a challenge persisting in atomic, molecular, and optical (AMO) laser physics.

## ACKNOWLEDGMENTS

Sandia National Laboratories is a multimission laboratory managed and operated by National Technology and Engineering Solutions of Sandia, LLC, a wholly owned subsidiary of Honeywell International Inc., for the U.S. Department of Energy's National Nuclear Security Administration under Contract No. DE-NA0003525. This work was performed, in part, at the Center for Integrated Nanotechnologies, an Office of Science User Facility operated for the U.S. Department of Energy (DOE) Office of Science. We acknowledge King Abdullah University of Science and Technology (KAUST) under Award Nos. RFS-OfP2023-5558, ORA-2022-5314, ORA-2022-5313, and SDAIA-KAUST Center of Excellence in Data Science and Artificial Intelligence (SDAIA-KAUST AI). Frédéric Grillot acknowledges the support of the Institut Mines-Télécom.

## AUTHOR DECLARATIONS

### Conflict of Interest

The authors have no conflicts to disclose.

### Author Contributions

A.P. and W.W.C. contributed equally to this paper.

**Artem Prokoshin:** Conceptualization (equal); Investigation (equal); Writing – original draft (equal). **Weng W. Chow:** Conceptualization (lead); Investigation (lead); Writing – original draft (equal). **Bozhang Dong:** Investigation (equal). **Frederic Grillot:** Supervision (equal). **John Bowers:** Supervision (equal); Writing – review & editing (equal). **Yating Wan:** Conceptualization (equal); Supervision (equal); Writing – review & editing (equal).

## DATA AVAILABILITY

The data that support the findings of this study are available from the corresponding author upon reasonable request.

## REFERENCES

- P. F. Liao and P. Kelley, *Quantum Well Lasers* (Elsevier, 2012).
- L. A. Coldren, S. W. Corzine, and M. L. Mashanovitch, *Diode Lasers and Photonic Integrated Circuits* (John Wiley & Sons, 2012).
- Y. Arakawa and H. Sakaki, "Multidimensional quantum well laser and temperature dependence of its threshold current," *Appl. Phys. Lett.* **40**, 939–941 (1982).
- D. Bimberg and U. W. Pohl, "Quantum dots: Promises and accomplishments," *Mater. Today* **14**, 388–397 (2011).
- V. M. Ustinov, *Quantum Dot Lasers* (Oxford University Press, 2003), Vol. 11.
- C. Shang, Y. Wan, J. Selvidge, E. Hughes, R. Herrick, K. Mukherjee, J. Duan, F. Grillot, W. W. Chow, and J. E. Bowers, "Perspectives on advances in quantum dot lasers and integration with Si photonic integrated circuits," *ACS Photonics* **8**, 2555–2566 (2021).
- J. C. Norman, D. Jung, Z. Zhang, Y. Wan, S. Liu, C. Shang, R. W. Herrick, W. W. Chow, A. C. Gossard, and J. E. Bowers, "A review of high-performance quantum dot lasers on silicon," *IEEE J. Quantum Electron.* **55**, 2000511 (2019).
- C. Henry, "Theory of the linewidth of semiconductor lasers," *IEEE J. Quantum Electron.* **18**, 259–264 (1982).
- M. W. Fleming and A. Mooradian, "Fundamental line broadening of single-mode (GaAl)As diode lasers," *Appl. Phys. Lett.* **38**, 511–513 (1981).
- A. Ukhonov, A. Stintz, P. Eliseev, and K. Malloy, "Comparison of the carrier induced refractive index, gain, and linewidth enhancement factor in quantum dot and quantum well lasers," *Appl. Phys. Lett.* **84**, 1058–1060 (2004).
- V. Vassiliev, V. Velichansky, V. Ilchenko, M. Gorodetsky, L. Hollberg, and A. Yarovsky, "Narrow-line-width diode laser with a high-Q microsphere resonator," *Opt. Commun.* **158**, 305–312 (1998).
- B. Li, W. Jin, L. Wu, L. Chang, H. Wang, B. Shen, Z. Yuan, A. Feshali, M. Paniccia, K. J. Vahala, and J. E. Bowers, "Reaching fiber-laser coherence in integrated photonics," *Opt. Lett.* **46**, 5201–5204 (2021).
- Y. Fan, A. van Rees, P. J. Van der Slot, J. Mak, R. M. Oldenbeuving, M. Hoekman, D. Gekus, C. G. Roeloffzen, and K.-J. Boller, "Hybrid integrated InP-Si<sub>3</sub>N<sub>4</sub> diode laser with a 40-Hz intrinsic linewidth," *Opt. Express* **28**, 21713–21728 (2020).
- W. Jin, Q.-F. Yang, L. Chang, B. Shen, H. Wang, M. A. Leal, L. Wu, M. Gao, A. Feshali, M. Paniccia *et al.*, "Hertz-linewidth semiconductor lasers using cmos-ready ultra-high-Q microresonators," *Nat. Photonics* **15**, 346–353 (2021).
- K. Liu, N. Chauhan, J. Wang, A. Isichenko, G. M. Brodnik, P. A. Morton, R. O. Behunin, S. B. Papp, and D. J. Blumenthal, "36 Hz integral linewidth laser based on a photonic integrated 4.0 m coil resonator," *Optica* **9**, 770–775 (2022).
- C. Xiang, W. Jin, O. Terra, B. Dong, H. Wang, L. Wu, J. Guo, T. J. Morin, E. Hughes, J. Peters *et al.*, "3D integration enables ultralow-noise isolator-free lasers in silicon photonics," *Nature* **620**, 78–85 (2023).
- Q. Su, F. Wei, C. Chen, Z. Fang, H. Pi, Y. Sun, F. Yang, A. Stroganov, H. Wu, G. Xin *et al.*, "A self-injection locked laser based on high-Q micro-ring resonator with adjustable feedback," *J. Lightwave Technol.* **41**, 6756 (2023).
- W. Liang, D. Eliyahu, V. S. Ilchenko, A. A. Savchenkov, A. B. Matsko, D. Seidel, and L. Maleki, "High spectral purity Kerr frequency comb radio frequency photonic oscillator," *Nat. Commun.* **6**, 7957 (2015).

- <sup>19</sup>A. S. Voloshin, N. M. Kondratiev, G. V. Lihachev, J. Liu, V. E. Lobanov, N. Y. Dmitriev, W. Weng, T. J. Kippenberg, and I. A. Bilenko, "Dynamics of soliton self-injection locking in optical microresonators," *Nat. Commun.* **12**, 235 (2021).
- <sup>20</sup>C. Xiang, J. Liu, J. Guo, L. Chang, R. N. Wang, W. Weng, J. Peters, W. Xie, Z. Zhang, J. Riemensberger *et al.*, "Laser soliton microcombs heterogeneously integrated on silicon," *Science* **373**, 99–103 (2021).
- <sup>21</sup>M. Corato-Zanarella, A. Gil-Molina, X. Ji, M. C. Shin, A. Mohanty, and M. Lipson, "Widely tunable and narrow-linewidth chip-scale lasers from near-ultraviolet to near-infrared wavelengths," *Nat. Photonics* **17**, 157–164 (2023).
- <sup>22</sup>L. Tang, L. Li, J. Li, and M. Chen, "Hybrid integrated ultralow-linewidth and fast-chirped laser for FMCW LiDAR," *Opt. Express* **30**, 30420–30429 (2022).
- <sup>23</sup>J. Li, B. Zhang, S. Yang, H. Chen, and M. Chen, "Robust hybrid laser linewidth reduction using Si<sub>3</sub>N<sub>4</sub>-based subwavelength hole defect assisted microring reflector," *Photonics Res.* **9**, 558–566 (2021).
- <sup>24</sup>A. E. Ulanov, T. Wildi, N. G. Pavlov, J. D. Jost, M. Karpov, and T. Herr, "Synthetic reflection self-injection-locked microcombs," *Nat. Photonics* **18**, 294–299 (2024).
- <sup>25</sup>B. Shen, X. Zhang, Y. Wang, Z. Tao, H. Shu, H. Chang, W. Li, Y. Zhou, Z. Ge, R. Chen *et al.*, "Reliable intracavity reflection for self-injection locking lasers and microcomb generation," *Photonics Res.* **12**, A41–A50 (2024).
- <sup>26</sup>R. Lang and K. Kobayashi, "External optical feedback effects on semiconductor injection laser properties," *IEEE J. Quantum Electron.* **16**, 347–355 (1980).
- <sup>27</sup>N. Kondratiev, V. Lobanov, A. Cherenkov, A. Voloshin, N. Pavlov, S. Koptyaev, and M. Gorodetsky, "Self-injection locking of a laser diode to a high-Q WGM microresonator," *Opt. Express* **25**, 28167–28178 (2017).
- <sup>28</sup>K. Aoyama, N. Yokota, and H. Yasaka, "Strategy of optical negative feedback for narrow linewidth semiconductor lasers," *Opt. Express* **26**, 21159–21169 (2018).
- <sup>29</sup>W. W. Chow, Y. Wan, J. E. Bowers, and F. Grillot, "Analysis of the spontaneous emission limited linewidth of an integrated III–V/SiN laser," *Laser Photonics Rev.* **16**, 2100620 (2022).
- <sup>30</sup>C. Xiang, J. Guo, W. Jin, L. Wu, J. Peters, W. Xie, L. Chang, B. Shen, H. Wang, Q.-F. Yang *et al.*, "High-performance lasers for fully integrated silicon nitride photonics," *Nat. Commun.* **12**, 6650 (2021).
- <sup>31</sup>R. Lang, M. O. Scully, and W. E. Lamb, Jr., "Why is the laser line so narrow? A theory of single-quasimode laser operation," *Phys. Rev. A* **7**, 1788 (1973).
- <sup>32</sup>K. Ebeling and L. Coldren, "Analysis of multielement semiconductor lasers," *J. Appl. Phys.* **54**, 2962–2969 (1983).
- <sup>33</sup>W. Chow, Z. Yang, G. Vawter, and E. Skogen, "Modulation response improvement with isolator-free injection-locking," *IEEE Photonics Technol. Lett.* **21**, 839–841 (2009).
- <sup>34</sup>M. B. Spencer and W. E. Lamb, Jr., "Laser with a transmitting window," *Phys. Rev. A* **5**, 884 (1972).
- <sup>35</sup>A. G. Fox and T. Li, "Resonant modes in a maser interferometer," *Bell Syst. Tech. J.* **40**, 453–488 (1961).
- <sup>36</sup>A. Taflov, S. C. Hagness, and M. Picket-May, "Computational electromagnetics: The finite-difference time-domain method," in *The Electrical Engineering Handbook*, 3 (Elsevier, 2005), p. 15.
- <sup>37</sup>Z.-H. Wang, W.-Q. Wei, Q. Feng, T. Wang, and J.-J. Zhang, "InAs/GaAs quantum dot single-section mode-locked lasers on Si (001) with optical self-injection feedback," *Opt. Express* **29**, 674–683 (2021).
- <sup>38</sup>J.-J. Chen, W.-Q. Wei, J.-L. Qin, B. Yang, J.-Z. Huang, Z.-H. Wang, T. Wang, C.-Y. Yu, and J.-J. Zhang, "Multi-wavelength injection locked semiconductor comb laser," *Photonics Res.* **10**, 1840–1847 (2022).
- <sup>39</sup>W. W. Chow and S. W. Koch, *Semiconductor-Laser Fundamentals: Physics of the Gain Materials* (Springer Science & Business Media, 2013).
- <sup>40</sup>W. W. Chow and S. Reitzenstein, "Quantum-optical influences in optoelectronics—An introduction," *Appl. Phys. Rev.* **5**, 041302 (2018).
- <sup>41</sup>W. W. Chow, A. Y. Liu, A. C. Gossard, and J. E. Bowers, "Extraction of inhomogeneous broadening and nonradiative losses in InAs quantum-dot lasers," *Appl. Phys. Lett.* **107**, 171106 (2015).
- <sup>42</sup>Z. Zhang, D. Jung, J. C. Norman, P. Patel, W. W. Chow, and J. E. Bowers, "Effects of modulation *p* doping in InAs quantum dot lasers on silicon," *Appl. Phys. Lett.* **113**, 061105 (2018).
- <sup>43</sup>Y. Wan, C. Xiang, J. Guo, R. Koscica, M. Kennedy, J. Selvidge, Z. Zhang, L. Chang, W. Xie, D. Huang *et al.*, "High speed evanescent quantum-dot lasers on Si," *Laser Photonics Rev.* **15**, 2100057 (2021).
- <sup>44</sup>B. Dong, Y. Wan, W. W. Chow, C. Shang, A. Prokoshin, E. Alkhazraji, R. Koscica, H. Wang, and J. E. Bowers, "Turnkey locking of quantum-dot lasers directly grown on silicon," *Nat. Photonics* **18**, 669–676 (2024).
- <sup>45</sup>A. L. Schawlow and C. H. Townes, "Infrared and optical masers," *Phys. Rev.* **112**, 1940 (1958).
- <sup>46</sup>J. Duan, B. Dong, W. W. Chow, H. Huang, S. Ding, S. Liu, J. C. Norman, J. E. Bowers, and F. Grillot, "Four-wave mixing in 1.3  $\mu\text{m}$  epitaxial quantum dot lasers directly grown on silicon," *Photonics Res.* **10**, 1264–1270 (2022).
- <sup>47</sup>W. W. Chow, S. Liu, Z. Zhang, J. E. Bowers, and M. Sargent, "Multimode description of self-mode locking in a single-section quantum-dot laser," *Opt. Express* **28**, 5317–5330 (2020).
- <sup>48</sup>W. W. Chow and F. Jahnke, "On the physics of semiconductor quantum dots for applications in lasers and quantum optics," *Prog. Quantum Electron.* **37**, 109–184 (2013).
- <sup>49</sup>W. Chow, A. Knorr, S. Hughes, A. Girndt, and S. Koch, "Carrier correlation effects in a quantum-well semiconductor laser medium," *IEEE J. Sel. Top. Quantum Electron.* **3**, 136–141 (1997).
- <sup>50</sup>A. W. Fang, E. Lively, Y.-H. Kuo, D. Liang, and J. E. Bowers, "A distributed feedback silicon evanescent laser," *Opt. Express* **16**, 4413–4419 (2008).
- <sup>51</sup>L. A. Lugiato and R. Lefever, "Spatial dissipative structures in passive optical systems," *Phys. Rev. Lett.* **58**, 2209 (1987).
- <sup>52</sup>E. Alkhazraji, W. W. Chow, F. Grillot, J. E. Bowers, and Y. Wan, "Linewidth narrowing in self-injection-locked on-chip lasers," *Light: Sci. Appl.* **12**, 162 (2023).
- <sup>53</sup>A. Koulas-Simos, G. Sinatkas, T. Zhang, J.-L. Xu, W. E. Hayenga, Q. Kan, R. Zhang, M. Khajavikhan, C.-Z. Ning, and S. Reitzenstein, "Extraction of silver losses at cryogenic temperatures through the optical characterization of silver-coated plasmonic nanolasers," *Opt. Express* **30**, 21664–21678 (2022).